MATERIALS SCIENCE

Boosting external quantum efficiency to 38.6% of sky-blue delayed fluorescence molecules by optimizing horizontal dipole orientation

Yan Fu[1†], Hao Liu[1†], Dezhi Yang[1], Dongge Ma[1], Zujin Zhao[1]*, Ben Zhong Tang[1,2,3]

To achieve high electroluminescence efficiency, great efforts are devoted to enhancing photoluminescence quantum yield (Φ_{PL}) and exciton utilization of luminescent molecule, while another important factor, light out-coupling efficiency (η_{out}), receives less attention in molecule design. Here, we focus on horizontal dipole orientation engineering of the molecule to increase η_{out} and external quantum efficiency (η_{ext}). A series of tailor-made luminescent molecules consisting of an electron-accepting carbonyl core plus double electron-donating groups of spiro[acridine-9,9′-fluorene] and carbazole derivatives [e.g., 1,3,5-tri(carbazol-9-yl)benzene] are developed and systematically investigated. These molecules hold distinguished merits of strong sky-blue delayed fluorescence with excellent Φ_{PL} values, large horizontal dipole ratios, and balanced bipolar carrier transport, which furnish record-high η_{ext} values of up to 26.1 and 38.6% in nondoped and doped sky-blue organic light-emitting diodes (OLEDs), respectively. Moreover, the state-of-the-art nondoped hybrid white OLED and all-fluorescence single-emitting layer white OLED are also realized, demonstrating great potentials in OLED industry of these molecules.

INTRODUCTION

As a promising display technique, organic light-emitting diodes (OLEDs) have attracted continuously increasing interests from academia and industry (*1*–*3*). To realize superb performances of OLEDs for commercial application, the developments of organic functional materials and device fabrication technologies are of critical importance. In general, the external quantum efficiency (η_{ext}) of OLED is the product of internal quantum efficiency (η_{int}) and light out-coupling ratio (η_{out}). Because η_{int} is determined by photoluminescence (PL) quantum yield (Φ_{PL}), exciton utilization efficiency (η_r), and carrier balance factor (γ), tremendous efforts have been devoted to exploring luminescent materials with high values in these aspects. Considerable current research interest is focused on purely organic luminescent materials with thermally activated delayed fluorescence (TADF), owing to their excellent theoretical η_r values of 100% by virtue of reverse intersystem crossing (RISC) process (*2*–*15*). The twisted electron donor (D)–acceptor (A) structures of TADF emitters may also bring about bipolar carrier transport ability and thus a high γ value. However, even if the molecule has a high η_{int} value of nearly 100%, for bottom-emitting OLED, the η_{out} value is generally in the range of 20 to 30%, corresponding to a top limit of 30% for η_{ext} (*16*, *17*). From this point of view, there is still much room for further improvement of η_{ext} by enhancing η_{out}.

In addition to adopting light extraction techniques, such as microlens arrays (*18*, *19*), scattering layers (*20*, *21*), and corrugated structures (*22*, *23*), raising horizontal dipole ratio ($\Theta_{//}$) is a feasible molecular engineering approach to reduce optical loss and enhance η_{out}. Elongating molecular conjugation along the direction of transition dipole moment (*24*–*27*) and expanding molecular plane where the transition dipole moment lies (*2*, *28*–*30*) are two major molecule design strategies in the literatures, but often at the cost of sacrificing emission color and efficiency of TADF emitters because of varied internal D-A interaction strength or strong intermolecular interactions in the aggregated state. To address this issue, recent studies proposed that the incorporation of spiro-shaped donor to create D-A backbones for TADF emitters could effectively enhance $\Theta_{//}$ without causing serious emission quenching (*24*, *31*–*33*), due to high steric hindrance. On the other hand, Byeon *et al.* (*30*) successfully realized nearly 100% horizontal dipole orientation of TADF emitters by increasing donor plane with carbazole units, but the energy level and emission color were greatly dependent on the number of carbazole units. Xiang *et al.* (*29*) succeeded in efficient modulation of horizontal dipole orientation without affecting electronic structures by the expansion of acceptor plane of TADF emitters and obtained highly efficient green OLEDs.

Taking the above into consideration, here, we wish to report the design and synthesis of a series of tailor-made luminogenic molecules with strong delayed fluorescence for highly efficient sky-blue OLEDs (Fig. 1A). In these molecules, carbonyl is selected as the electron-accepting core because carbonyl can undergo n-π* transition, availing the spin-orbit coupling (SOC) and thus promoting RISC process (*34*). Electron-donating spiro[acridine-9,9′-fluorene] (SFAC) is connected to one side of carbonyl core via a phenyl bridge to construct a D-A framework for the generation of delayed fluorescence. In addition, hole-transporting functional groups of 9-phenylcarbazole (CP), 1,3-di(carbazol-9-yl)benzene (*m*CP), and 1,3,5-tri(carbazol-9-yl) benzene (TCP) are introduced to the other side of carbonyl core to facilitate the balance of carrier injection and transport of the molecules. It is envisioned that, in addition to the spiro group SFAC (*24*), the presence of these carbazole-based functional groups can enlarge molecular plane for transition dipole moment and thus have supplemental effect for optimizing $\Theta_{//}$ values. Meanwhile, these rigid and space-demanded functional groups (e.g., SFAC and TCP) can also reduce intramolecular motion and inhibit intermolecular π-π

[1]State Key Laboratory of Luminescent Materials and Devices, Guangdong Provincial Key Laboratory of Luminescence from Molecular Aggregates, South China University of Technology, Guangzhou 510640, China. [2]Shenzhen Institute of Aggregate Science and Technology, School of Science and Engineering, Chinese University of Hong Kong, Shenzhen, Guangdong 518172, China. [3]AIE Institute, Guangzhou Development District, Huangpu, Guangzhou 510530, China.
*Corresponding author. Email: mszjzhao@scut.edu.cn
†These authors contributed equally to this work.

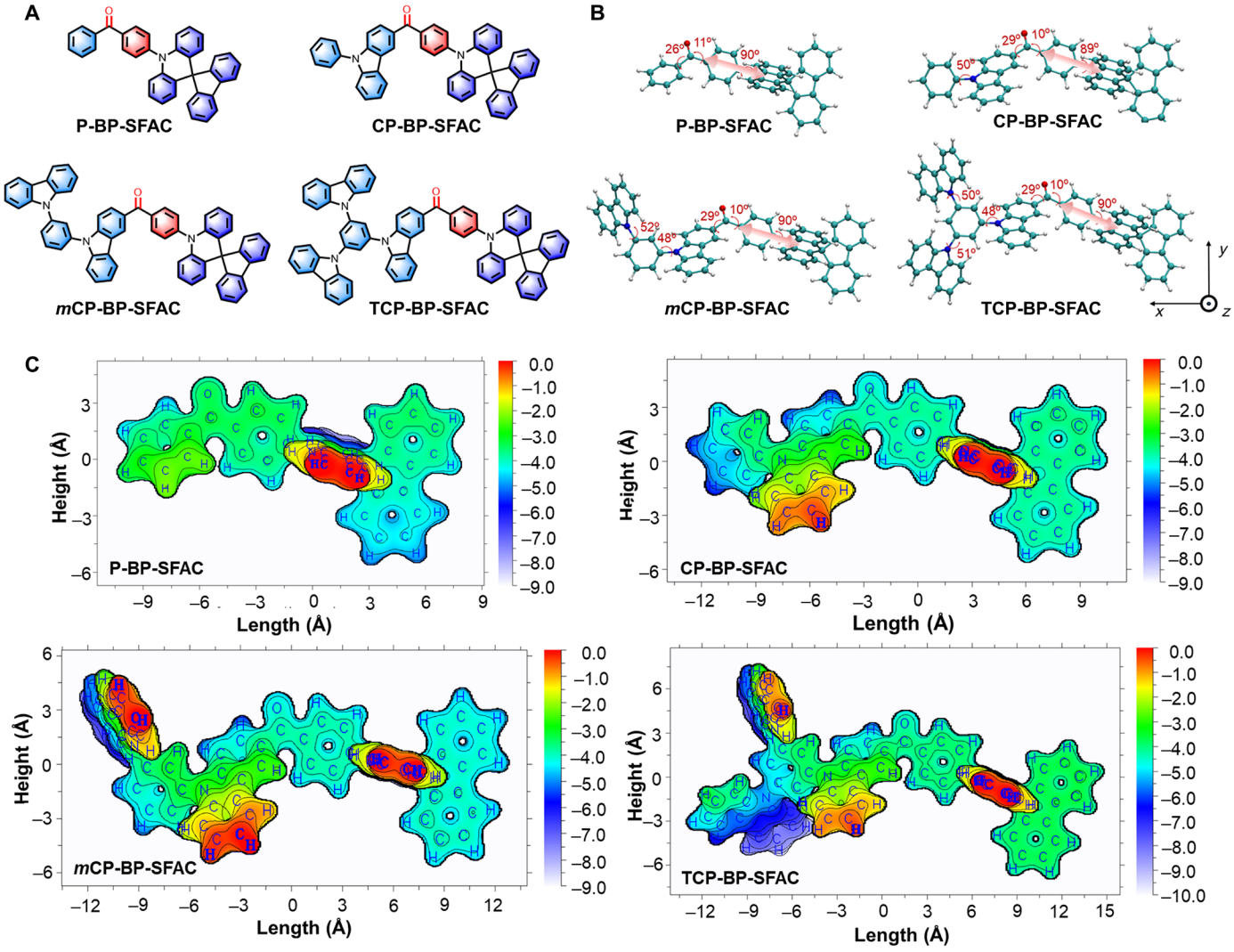

Fig. 1. New molecules studied in this work. (**A**) Chemical structures and (**B**) geometrical structures of the new molecules, optimized by time-dependent density functional theory (DFT). Dihedral angles are indicated in the geometrical structures, and transition dipole moment of S_1 state is indicated by red arrow. (**C**) Surface distance projection maps in the *x-y* plane of P-BP-SFAC, CP-BP-SFAC, *m*CP-BP-SFAC, and TCP-BP-SFAC.

interactions, ensuring efficient emissions in solid films (*35*). As expected, the generated molecules not only exhibit strong sky-blue delayed fluorescence with excellent Φ_{PL} values reaching 99% but also prefer horizontal dipole orientation in film states with large $\Theta_{//}$ values of up to 88.0%. On the basis of these new molecules, efficient sky-blue nondoped OLEDs are fabricated, furnishing outstanding η_{ext} values of 26.1% and small efficiency roll-offs. Moreover, superb sky-blue doped OLEDs with even higher η_{ext} values of up to 38.6% are achieved, which could be the most efficient OLED with similar color reported so far. Further, nondoped hybrid white OLED and all-fluorescence single-emitting layer white OLED with the state-of-the-art performances are realized on the basis of the new sky-blue molecules.

RESULTS

Synthesis and characterization

The new luminogenic molecules (CP-BP-SFAC, *m*CP-BP-SFAC, and TCP-BP-SFAC) and a control molecule (P-BP-SFAC) were prepared facilely according to the straightforward synthetic routes outlined in fig. S1. The detailed synthetic procedures and characterization data are described in the Supplementary Materials. CP-BP-SFAC, *m*CP-BP-SFAC, and TCP-BP-SFAC enjoy brilliant thermal stability (fig. S2), with high decomposition temperatures of 504°, 559°, and 589°C, respectively, which are much higher than that of P-BP-SFAC (371°C), disclosing that the introduction of carbazole units has greatly improved the thermal stability of the molecules. No clear glass-transition temperatures are observed for these molecules, indicative of inconspicuous thermal transitions and thus good morphological stability. Moreover, these molecules have reversible oxidation and reduction processes, as measured by cyclic voltammetry (fig. S3), demonstrating their good electrochemical stability. From the onsets of oxidation and reduction waves, the energy levels of the highest occupied molecular orbitals (HOMOs) and the lowest unoccupied molecular orbitals (LUMOs) are obtained. CP-BP-SFAC, *m*CP-BP-SFAC, and TCP-BP-SFAC have approximate LUMO energy levels of ca. −2.67 eV, and HOMO ones of ca. −5.36 eV, which

are very close to those of P-BP-SFAC (−2.75 and −5.36 eV), implying that LUMO and HOMO energy levels are mainly determined by the D-A framework based on carbonyl and SFAC.

The geometrical and electronic structures of these molecules are studied by theoretical calculation. In optimized molecular structures, the carbonyl and SFAC are connected in a highly twisted conformation via the phenyl bridge, with large torsion angles of ~90° between SFAC and phenyl bridge (Fig. 1B), which is favored for the separation of HOMOs and LUMOs to endow the molecules with small energy splitting between lowest singlet (S_1) and triplet (T_1) states (ΔE_{ST}). On the contrary, the carbazole groups are conjugated better to carbonyl core in CP-BP-SFAC, *m*CP-BP-SFAC, and TCP-BP-SFAC with small torsion angles of 26° to 29°. In consequence, the HOMOs are mainly concentrated at the acridine segment, while the LUMOs are distributed on carbonyl core, phenyl bridge, and part of carbazole unit adjacent to carbonyl core. These almost the same transition orbital distributions on the D-A framework based on carbonyl and SFAC moieties as well as very close energy levels of HOMOs and LUMOs imply the similar PL property. In addition, because of the separated distribution of HOMOs and LUMOs, the theoretical ΔE_{ST} values are calculated to be 0.106, 0.080, and 0.061 eV for CP-BP-SFAC, *m*CP-BP-SFAC, and TCP-BP-SFAC, respectively, which are small enough for the occurrence of RISC process (*36*).

The calculated spin-density distributions of T_1 states (TSDD) indicate that the triplet excitons are mainly located on the carbonyl core and adjacent phenyl rings, while barely on the peripheral rigid aromatic groups, probably due to the low-lying energy level of carbonyl core (Fig. 2). As the increase of carbazole units, the entire molecules become more space-demanded, which can protect the excitons on the central carbonyl core from getting close, namely, the peripheral rigid aromatic groups without obvious exciton distributions can act as a defense against exciton annihilation. On the other hand, the transition dipole moments of all the molecules are calculated to be preferentially oriented along the molecular axis (in the *x*-*y* plane) of the D-A framework based on carbonyl and SFAC (Fig. 1B). The introduction of carbazole units can expand the effective projected area in the *x*-*y* plane (Fig. 1C) for the transition dipole moment to lie in, suggesting a positive effect on horizontal dipole orientation. However, the enhancement of projected areas by *m*CP and TCP are somewhat limited relative to that of CP, because the additional carbazole units in *m*CP and TCP are actually highly twisted out of the molecular plane of transition dipole moment, implying similar effects from CP, *m*CP, and TCP for horizontal dipole orientation.

CP-BP-SFAC, *m*CP-BP-SFAC, and TCP-BP-SFAC show similar absorption maxima at 335 to 337 nm in tetrahydrofuran (THF) solutions, assigned to the π-π* transitions of the molecules. The intramolecular charge transfer (ICT) states are reflected as absorption tails extending to 430 nm rather than discernible absorption peaks, indicating that the ICT effect should be weak in these molecules. On the contrary, P-BP-SFAC exhibits an apparent absorption band with a peak at about 377 nm, indicative of a stronger ICT effect. Similar absorption spectral profiles are also observed in nonpolar toluene solutions (fig. S4). These findings disclose that the electron-withdrawing ability of the carbonyl core has been weakened by the direct connection to the 3-position of electron-donating carbazole group, leading to decreased ICT effect between carbonyl and SFAC. In comparison to strong ICT effect, the relatively weak ICT effect is actually more favorable to achieve stronger and bluer PL emissions.

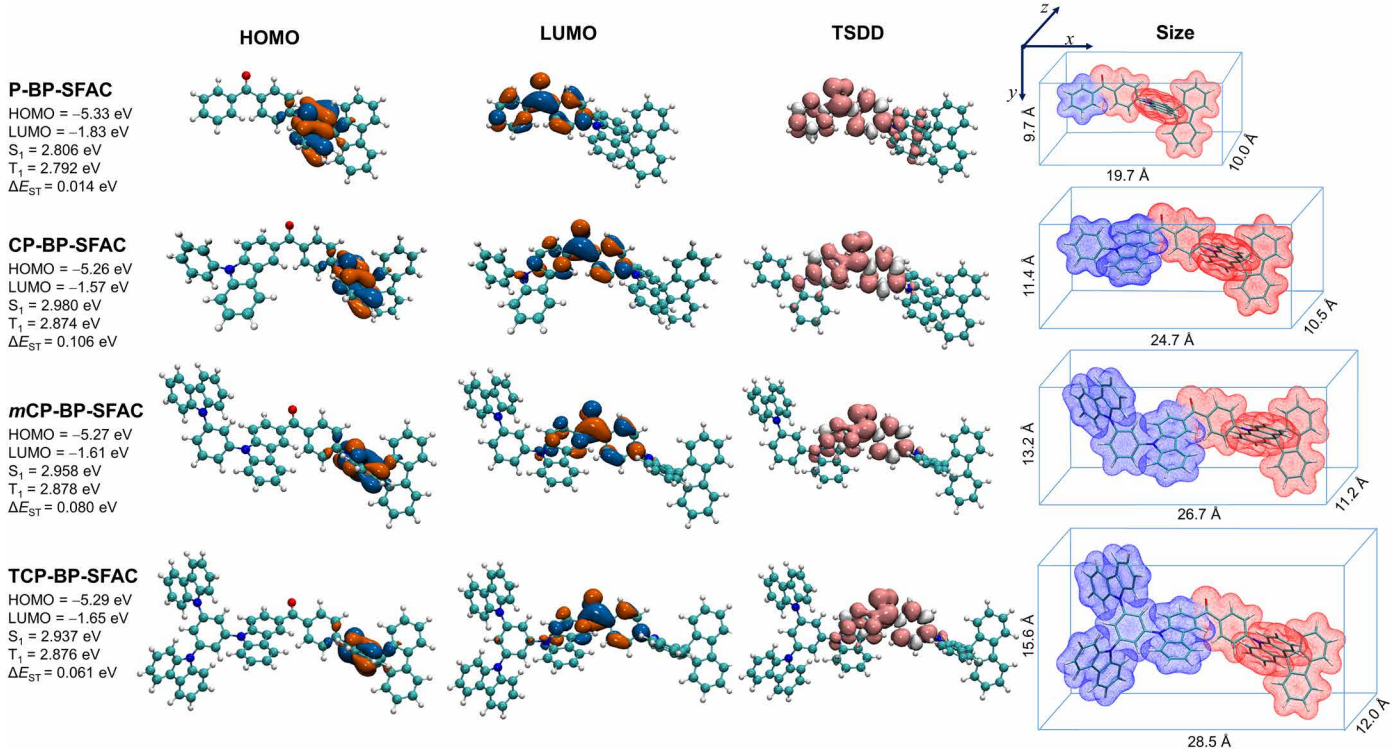

Fig. 2. Theoretical calculations of P-BP-SFAC, CP-BP-SFAC, *m*CP-BP-SFAC, and TCP-BP-SFAC. Frontier molecular orbital distributions, spin-density distributions of T_1 states (TSDD), and the length, width, and height of the molecules. The optimized geometrical and electronic structures were calculated by PBE0-D3/6-31G (d, p).

CP-BP-SFAC, *m*CP-BP-SFAC, and TCP-BP-SFAC exhibit strong sky-blue delayed fluorescence in neat films, with PL peaks at ~483 nm and delayed fluorescence lifetimes ($\tau_{delayed}$) of 5.4 to 5.7 μs. The Φ_{PL} values are increased from 77% of CP-BP-SFAC to 86% of *m*CP-BP-SFAC and to 92% of TCP-BP-SFAC. The doped films of these molecules in diphenyl-4-triphenylsilylphenyl-phosphine oxide (DPEPO) host at concentrations of 20 or 25 weight % (wt %) exhibit similar PL peaks at 478 to 482 nm, close $\tau_{delayed}$ values of 5.5 to 5.6 μs, and outstanding Φ_{PL} values reaching 99%. These Φ_{PL} and $\tau_{delayed}$ values in both neat and doped films are much larger than those in THF or toluene solutions (Table 1). Similar enhancements in emission intensity and lifetime can also be detected in their nanoaggregates formed by adding a large amount of water into THF solutions (Fig. 3C, figs. S5 and S6, and Table 1). The interesting phenomenon of obviously enhanced delayed fluorescence in films or nanoaggregates can be attributed to the restriction of intramolecular motion and molecular structure rigidification by spatial constraint, which blocks nonradiative decay of excited states, and thus facilitates RISC process and radiative decay (*37*–*39*). By increasing temperature from 77 to 300 K, the proportion of delayed components of these molecules in both neat and doped films is enhanced apparently, disclosing that the delayed fluorescence can be promoted by thermal energy, namely, TADF characteristic (Fig. 3D, figs. S7 and S8, table S1).

CP-BP-SFAC, *m*CP-BP-SFAC, and TCP-BP-SFAC have quite close values of PL peak, Φ_{PL}, $\tau_{delayed}$, and other relevant constants in RISC process (table S2) in doped films, and similar phenomenon is also observed for these molecules in solutions. However, the Φ_{PL} values of CP-BP-SFAC, *m*CP-BP-SFAC, and TCP-BP-SFAC in neat films are enhanced progressively along with the increase of carbazole unit. These findings further validate that, at the molecularly dispersed states, the photophysical properties of these molecules are mainly determined by the D-A framework based on carbonyl and SFAC, and the increase of carbazole units shows little interference. However, in neat films, the presence of more carbazole units, particularly the star-burst TCP, is conducive to preventing emission quenching and improving emission intensity, rendering a highest Φ_{PL} value of 92% of TCP-BP-SFAC. These experimental results are in good agreement with the theoretical calculations as discussed above.

Host tuning effect on ΔE_{ST}

CP-BP-SFAC, *m*CP-BP-SFAC, and TCP-BP-SFAC show ΔE_{ST} values of 0.086, 0.095, and 0.094 eV in neat films (fig. S9) and 0.057, 0.058, and 0.059 eV in doped films with a DPEPO host (fig. S10), measured from the fluorescence and phosphorescence spectra at 77 K. These small ΔE_{ST} values can ensure the occurrence of RISC process and thus delayed fluorescence. However, in comparison with the neat films, the doped films have smaller ΔE_{ST} values and higher ratios of delayed components (table S2), disclosing that a DPEPO host benefits the delayed fluorescence of these molecules. To further confirm the ΔE_{ST} values, TCP-BP-SFAC is taken as an example to evaluate the ΔE_{ST} values of its neat and doped films by fitting an Arrhenius plot according to $k_{RISC} \propto \exp.(\Delta E_{ST}/k_B T)$ (*40*), where k_{RISC}, k_B, and T denote the RISC rate constant, Boltzmann constant, and temperature, respectively. The ΔE_{ST} values are estimated to be 0.094 and 0.052 eV for neat film and doped film, respectively, which are quite close to the ΔE_{ST} values obtained from the fluorescence and phosphorescence spectra (fig. S11).

As shown in table S3, the decrease of ΔE_{ST} values in doped films results from the more increments of energy levels of T_1 than S_1 states, which can be attributed to the different impacts of a DPEPO host on S_1 and T_1 transitions of these molecules. Such kind of host tuning effect in this system is virtually associated with the different polarities and the valence shell transition types of S_1 and T_1 states. The theoretical calculation results disclose that the S_1 states of these molecules are dominated by π-π* transition, while the T_1 states are governed by n-π* transition (Fig. 4) (*41*). The n orbital is sensitive to the changes in matrix polarity because of its high polarity caused by strong electron-withdrawing oxygen atom in C═O double bond, but the π orbital is relatively polarity insensitive because of the evenly distributed electron cloud (*42*). Therefore, the energy levels of T_1 states can be changed in a larger degree than those of S_1 states when the matrix polarity is altered.

On the other hand, the calculated molecular polarity index (MPI) values of these molecules in S_1 and T_1 states are 14.68 to 19.95 and 8.65 to 10.01 kcal mol^{-1}, respectively (table S4). The MPI value of a DPEPO host is 11.20 kcal mol^{-1}, which is smaller than those of S_1 states, but larger than those of T_1 states. Therefore, when these molecules are in S_1 states, the doped films with a DPEPO host have lower polarity than the neat films formed by these molecules. In consequence, the energy levels of S_1 states are increased. On the contrary, in T_1 states, the doped films have higher polarity than the neat films, resulting in enhanced energy levels as well. However, the increments of T_1 energy levels are larger than those of S_1 ones, leading to decreased ΔE_{ST} values in doped films finally (Fig. 5), which is in excellent agreement with the experimental measurement.

Table 1. Photophysical properties of P-BP-SFAC, CP-BP-SFAC, *m*CP-BP-SFAC, and TCP-BP-SFAC.

Emitter	THF/toluene*				Neat film/doped film†						
	λ_{abs} (nm)	λ_{em} (nm)	Φ_{PL}‡ (%)	<τ>§ (ns)	λ_{em} (nm)	Φ_{PL}‡ (%)	<τ>§ (μs)	$\tau_{delayed}$‖ (μs)	$R_{delayed}$¶ (%)	ΔE_{ST}# (meV)	$\Theta_{//}$** (%)
P-BP-SFAC	377/372	518/485	24/49	126/327	493/491	88/94	1.7/2.3	4.8/5.2	34.6/43.5	55/50	71.5/72.5
CP-BP-SFAC	335/342	507/475	36/31	499/414	482/481	77/99	1.7/2.4	5.4/5.5	33.0/44.6	86/57	86.5/84.5
*m*CP-BP-SFAC	337/338	509/475	36/33	262/448	484/478	86/99	1.8/2.4	5.5/5.5	33.0/43.0	95/58	87.5/86.0
TCP-BP-SFAC	336/337	512/476	26/40	143/568	483/482	92/99	1.6/2.5	5.7/5.6	27.2/43.9	94/59	85.5/88.0

*Measured in THF and toluene solutions (10^{-5} M) bubbled with nitrogen. †Doped films are 20 wt % P-BP-SFAC:DPEPO, 25 wt % CP-BP-SFAC:DPEPO, 20 wt % *m*CP-BP-SFAC:DPEPO, and 25 wt % TCP-BP-SFAC:DPEPO. ‡Absolute PL quantum yield determined by a calibrated integrating sphere under nitrogen at room temperature. §Mean fluorescence lifetime evaluated at 300 K under nitrogen. ‖Lifetime of delayed decay component evaluated at 300 K under nitrogen. ¶Proportion of delayed component evaluated at 300 K under nitrogen. #Estimated from the onsets of fluorescence and phosphorescence spectra at 77 K. **Horizontal emitting dipole ratio.

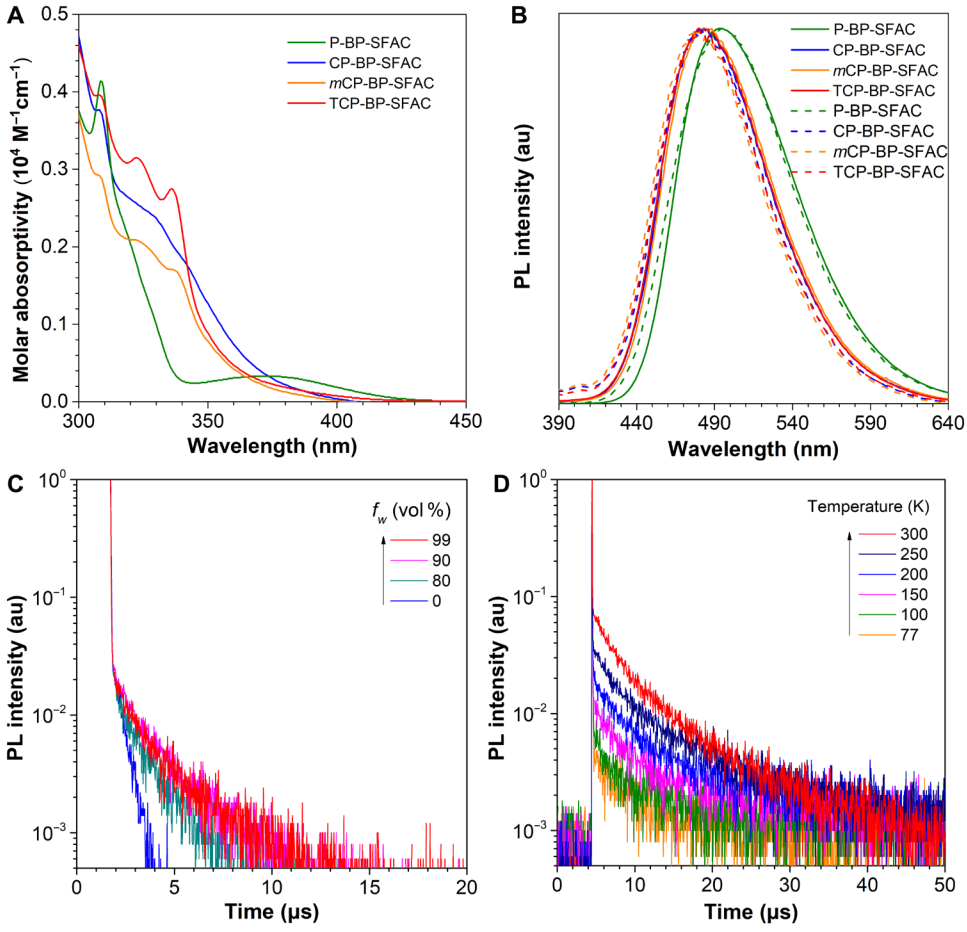

Fig. 3. Photophysical properties of P-BP-SFAC, CP-BP-SFAC, *m*CP-BP-SFAC, and TCP-BP-SFAC. (**A**) Absorption spectra in THF solutions (10^{-5} M). (**B**) PL spectra in neat films (solid line) and doped films (dash line) of P-BP-SFAC, CP-BP-SFAC, *m*CP-BP-SFAC, and TCP-BP-SFAC. (**C**) PL decay curves of TCP-BP-SFAC in THF/water mixtures with different water fractions (f_w) (10^{-5} M) and (**D**) temperature-dependent PL decay curves of 25 wt % TCP-BP-SFAC:DPEPO–doped film, measured under nitrogen. au, arbitrary units.

To verify the reliability of the account, a low-polar host TCP, which has a lower polarity (MPI = 8.42 kcal mol^{-1}) than those of DPEPO as well as TCP-BP-SFAC in the T_1 state (MPI = 8.72 kcal mol^{-1}), is chosen to fabricate doped film of TCP-BP-SFAC with a concentration of 25 wt %. Compared with the neat film, the doped film of TCP-BP-SFAC exhibits an obviously increased S_1 energy level, and the increment is much larger than that in the doped film with a DPEPO host. On the contrary, the T_1 energy level of the doped film is only slightly altered. Consequently, the ΔE_{ST} value of the doped film is greatly enhanced to 0.146 eV (fig. S10E). These results demonstrate that the host materials have a substantial tuning effect on the ΔE_{ST} values of the delayed fluorescence molecules.

Horizontal dipole orientation

The orientation of the transition dipole moments of these molecules in neat and doped films deposited on quartz substrates is investigated by using the angle-dependent *p*-polarized PL spectra *(28)*. TCP-BP-SFAC shows large $\Theta_{//}$ values of 85.5% in neat film and 88.0% in doped film, indicative of enhanced η_{out} values relative to those of common molecules with random dipole orientation (Fig. 6, A and B). The $\Theta_{//}$ values of P-BP-SFAC are 71.5% in neat film and 72.5% in doped film (Fig. 6, C and D), which are larger than those of common molecules but still smaller than those of TCP-BP-DMAC (9,9-dimethylacridine). On the other side, the $\Theta_{//}$ values of the other two control molecules P-BP-DMAC and TCP-BP-DMAC containing DMAC instead of SFAC are measured as 63.0 and 76.0%, respectively (fig. S12), rendering the same trend as that of P-BP-SFAC and TCP-BP-SFAC. These results demonstrate that the presence of TCP is conducive to horizontal dipole orientation, owing to the expanded molecular plane, where the transition dipole moment lies (*29*, *30*). Besides, the $\Theta_{//}$ values of P-BP-SFAC and TCP-BP-SFAC are also larger than those of P-BP-DMAC and TCP-BP-DMAC, verifying that the spiro group SFAC is beneficial for horizontal dipole orientation, which is consistent with the reported results (*24*). Therefore, it comes to a conclusion that the combined horizontal dipole orientation effects from SFAC and TCP endow a larger $\Theta_{//}$ value of TCP-BP-SFAC than those of P-BP-SFAC and TCP-BP-DMAC with individual effect from SFAC and TCP, respectively. CP-BP-SFAC and *m*CP-BP-SFAC also exhibit a high trend for horizontal dipole orientation with large $\Theta_{//}$ values similar to those of TCP-BP-SFAC in neat and doped films (Table 1 and figs. S12 and S13).

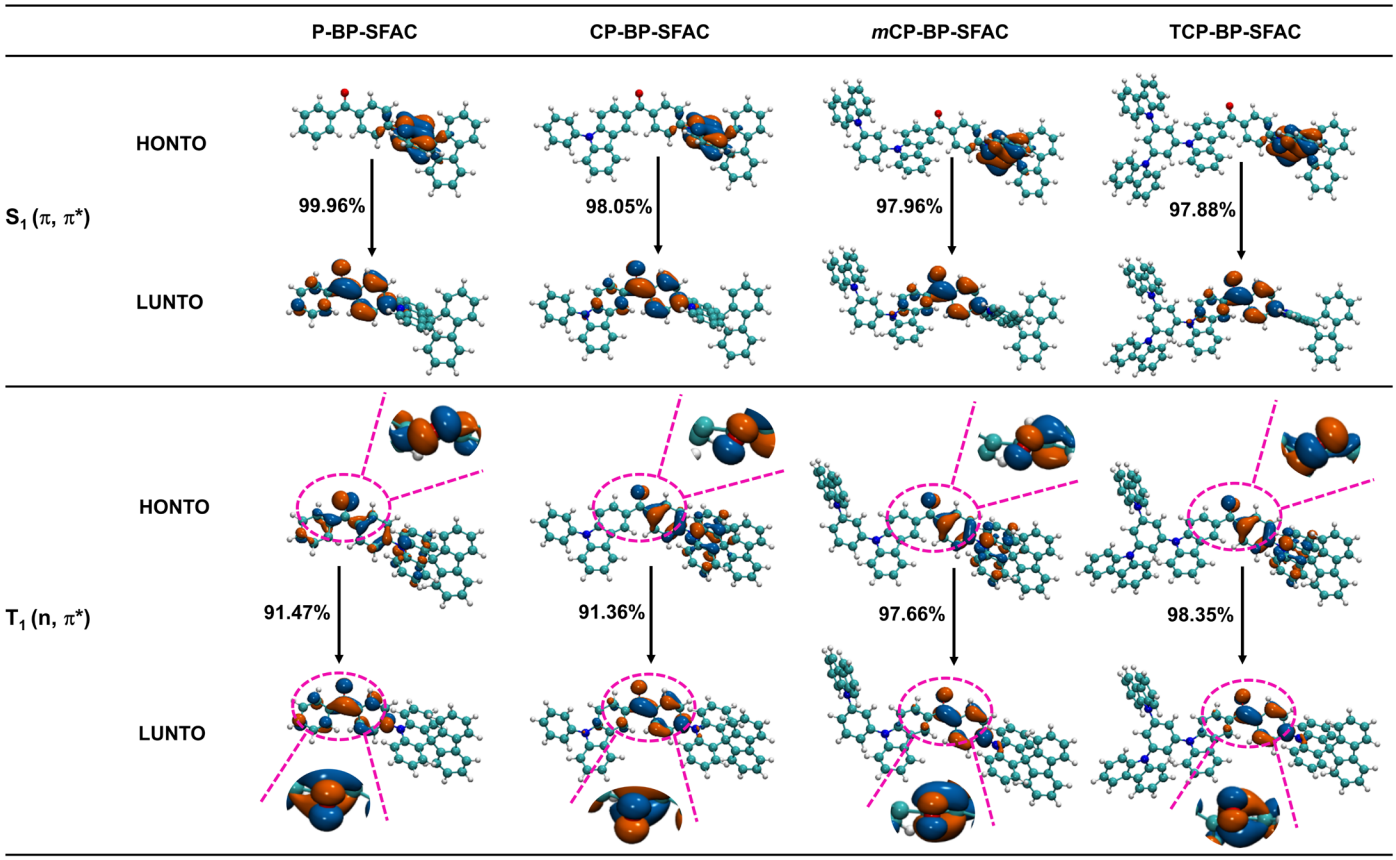

Fig. 4. Transition types of S_1 and T_1 states. Natural transition orbital (NTO) analysis of S_1 and T_1 states for P-BP-SFAC, CP-BP-SFAC, *m*CP-BP-SFAC, and TCP-BP-SFAC. The encircled and enlarged parts indicate the n orbital character.

Bipolar carrier transport

To investigate the impact of carbazole groups on the carrier transport behaviors of these molecules, their hole and electron mobilities are measured by the space-charge limited current (SCLC) method on the hole- and electron-only devices with configurations of indium tin oxide (ITO)/1,10-bis(di-4-tolylaminophenyl)cyclohexane (TAPC; 10 nm)/emitter (80 nm)/TAPC (10 nm)/Al and ITO/1,3,5-tri(m-pyrid-3-yl-phenyl)benzene (TmPyPB; 10 nm)/emitter (80 nm)/TmPyPB (10 nm)/LiF (1 nm)/Al, respectively, in which TAPC and TmPyPB function as buffer layers to shield off electrons and holes, respectively. As shown in Fig. 7, the hole and electron mobilities become close as the increase of carbazole units, and TCP-BP-SFAC shows an impressive balance in carrier mobility in a wide range of electric field from 4×10^4 to 1×10^6 V cm^{-1}. The eminent balanced bipolar carrier mobility should be beneficial to exciton recombination efficiency and exciton recombination zone located in the middle of the emitting layer.

Moreover, close survey on the hole and electron mobilities of these molecules unveils that the electron mobilities are only altered to a very small extent but the hole mobilities exhibit relatively large changes as the introduction of carbazole units. To gain a deep insight into the effects of carbazole units on the carrier mobilities, molecular orbitals and volumes are taken into consideration. As mentioned above, the distributions of the HOMOs and LUMOs of these molecules are almost the same. Hence, the difference in carrier mobility may be caused by other orbitals. In general, the energy gaps between the unoccupied orbitals are wider than those of the occupied orbitals as described by the variational principle, and furthermore, the antibonding nature of the unoccupied orbitals except the LUMOs makes them hardly contribute to electron mobility (*43*–*45*). Therefore, for these molecules, the electron mobilities are dominated by the LUMOs that are mainly located on central carbonyl and nearby fragments. Although the introduction of carbazole units can increase molecular volumes and affect molecular packing, the almost identical LUMO distributions and relatively long distances among electron-transporting carbonyl cores render only slight fluctuations in electron mobilities of these molecules.

As for the hole mobility, the calculation results show that, in addition to the HOMOs, the HOMO-1 orbitals of these molecules are able to contribute to hole mobility because their energy levels are relatively closer to those of HOMOs. The HOMO distributions are almost identical, but the HOMO-1 orbitals are located on different fragments (fig. S14). The HOMO-1 orbitals of P-BP-SFAC and CP-BP-SFAC are centered on fluorene units, while those of *m*CP-BP-SFAC and TCP-BP-SFAC are located on a peripheral carbazole of *m*CP and TCP moieties. The molecular volumes and stacking can have large impacts on the distances and interactions among peripheral fluorene and carbazole units than the central carbonyl. Given the same distributions of the HOMO and HOMO-1 orbitals of P-BP-SFAC and CP-BP-SFAC, the lower hole mobility of CP-BP-SFAC than P-BP-SFAC is probably caused by the looser stacking of CP-BP-SFAC due to its more branched conformation, which is unfavorable for

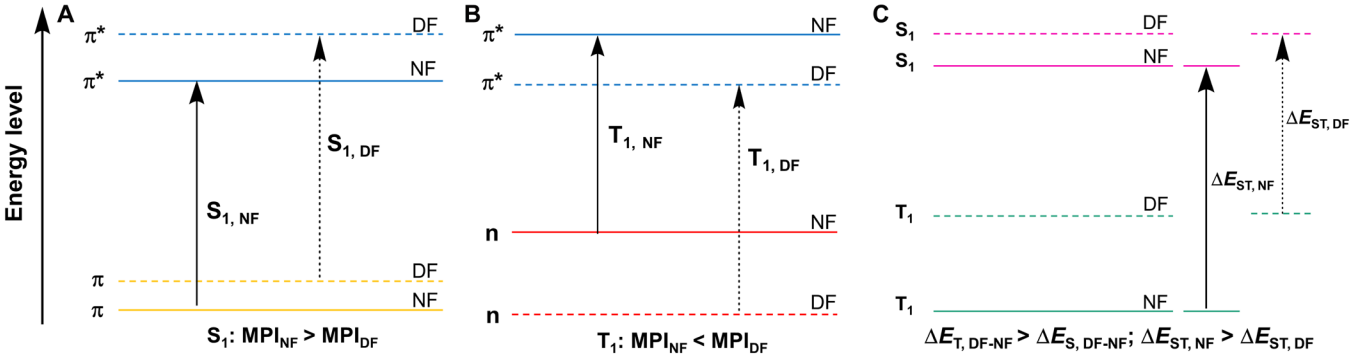

Fig. 5. The energy levels in neat film and doped film. The energy level changes of (**A**) S_1 and (**B**) T_1 states and (**C**) varied ΔE_{ST} values from neat films (NF) to doped films (DF) with a DPEPO host. MPI_{NF} and MPI_{DF} denote the MPI values in neat film and doped film, respectively. $\Delta E_{T,\,DF\text{-}NF}$ and $\Delta E_{S,\,DF\text{-}NF}$ denote the energy level changes of T_1 and S_1 states from neat film to doped film, respectively. $\Delta E_{ST,\,NF}$ and $\Delta E_{ST,\,DF}$ denote the ΔE_{ST} in neat film and doped film, respectively.

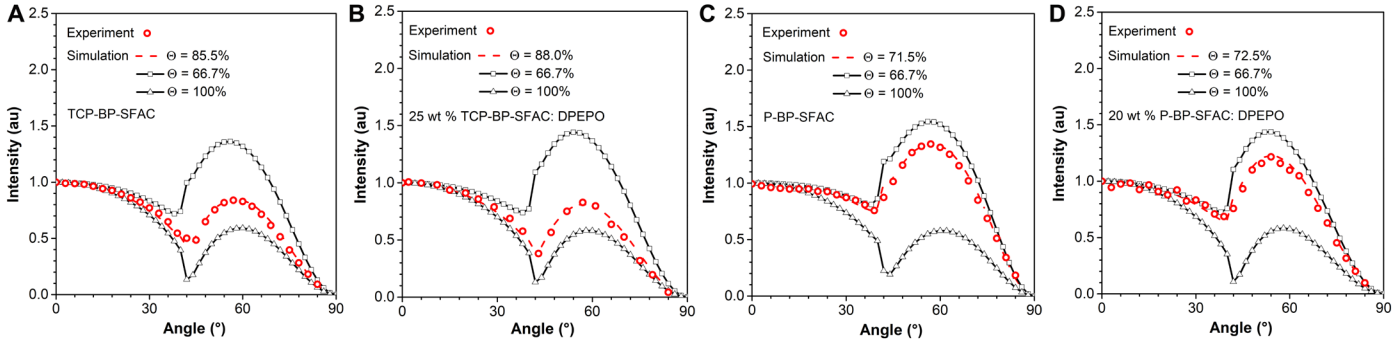

Fig. 6. The characterizations of horizontal dipole orientation by angle-dependent *p*-polarized PL spectra. Measured horizontal transition dipole moment ratios of neat and doped films of (**A** and **B**) TCP-BP-SFAC and (**C** and **D**) P-BP-SFAC.

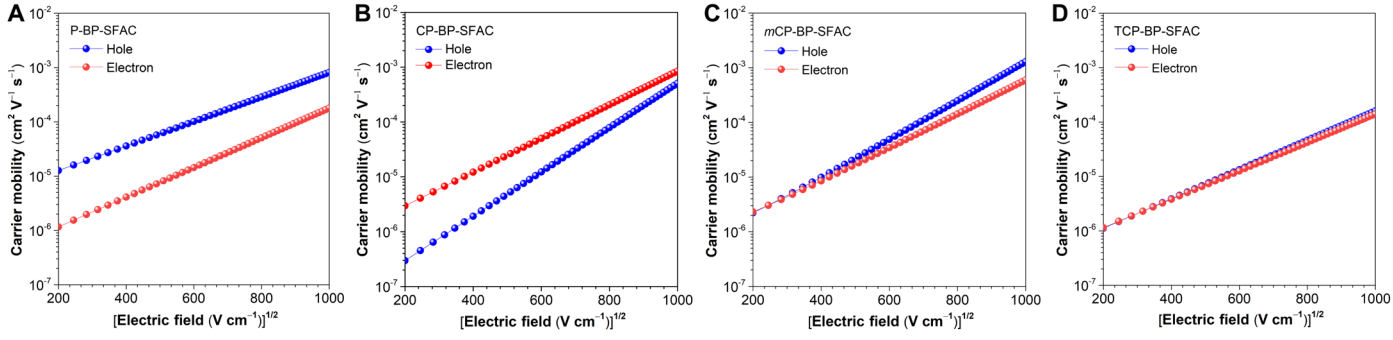

Fig. 7. The characterizations of bipolar carrier mobility by SCLC method. Electric field–dependent carrier mobility of (**A**) P-BP-SFAC, (**B**) CP-BP-SFAC, (**C**) *m*CP-BP-SFAC, and (**D**) TCP-BP-SFAC neat films in single-carrier devices.

hole mobility via a hopping model. This is also true for the slightly lower hole mobility of TCP-BP-SFAC than *m*CP-BP-SFAC. On the other hand, the lower hole mobility of CP-BP-SFAC than *m*CP-BP-SFAC is attributed to the weaker hole transport ability of fluorene than carbazole. In short, the introduction of carbazole units mainly changes the distribution of the HOMO-1 orbitals and the molecular packings, both of which can influence the carrier mobilities.

Electroluminescence performances

In view of the strong delayed fluorescence, horizontal dipole orientation, and balanced bipolar carrier mobility of these molecules in neat films, their electroluminescence (EL) performances in nondoped OLEDs are initially evaluated. The device configuration is ITO/hexaazatriphenylenehexacabonitrile (HATCN; 5 nm)/TAPC (50 nm)/tris[4-(carbazol-9-yl)phenyl]amine (TCTA; 5 nm)/*m*CP (5 nm)/emitter (20 nm)/DPEPO (5 nm)/TmPyPB (30 nm)/LiF (1 nm)/Al, in which the neat films of these molecules are used as emitting layers, and the functional layers of HATCN, TAPC, TCTA, and TmPyPB are adopted for hole injection, hole transport, hole buffer, and electron transport layers, respectively. *m*CP and DPEPO work as exciton blocking layer to confine the excitons within the emitting layer on account of their high T_1 energy levels (2.9 and 3.0 eV)

(*46*, *47*). These nondoped OLEDs can be turned on at low voltages of 2.7 to 2.8 V with high maximum luminance (L_{max}) values of 28,590 to 39,460 cd m^{-2}, indicative of facile carrier injection, balanced carrier transport, and efficient exciton recombination in devices (Fig. 8, B and C, and fig. S15A). The device of CP-BP-SFAC shows an EL peak at 490 nm and Commission Internationale de l'Eclairage coordinates ($CIE_{x,y}$) of (0.19, 0.36). Its maximum η_{ext} ($\eta_{ext,max}$), current efficiency ($\eta_{C,max}$), and power efficiency ($\eta_{P,max}$) are 22.5%, 51.2 cd A^{-1}, and 57.4 lm W^{-1}, respectively. The devices of *m*CP-BP-SFAC and TCP-BP-SFAC radiate strong sky-blue EL emissions with slightly blue-shifted peaks at 488 nm ($CIE_{x,y}$ = 0.17, 0.34) and provide excellent $\eta_{ext,max}$, $\eta_{C,max}$, and $\eta_{P,max}$ values of 25.0%, 53.8 cd A^{-1}, and 56.0 lm W^{-1} and 26.1%, 56.4 cd A^{-1}, and 63.3 lm W^{-1}, respectively. The device of TCP-BP-SFAC enjoys the best efficiency stability, whose η_{ext} remains as 23.8% at a high luminance of 1000 cd m^{-2}, equal to a small efficiency roll-off of 9.6%, which is much superior to that of P-BP-SFAC–based device (31.3%). According to the calculated results of TSDD, the space-demanded star-burst TCP can better suppress exciton annihilation via short-distance Dexter energy transfer. The perfectly balanced carrier transport of TCP-BP-SFAC makes exciton recombination occur as much as possible at the middle region of TCP-BP-SFAC layer and thus reduce exciton quenching at the interfaces of active layers. These factors are considered to account for the smallest efficiency roll-off of the nondoped device of TCP-BP-SFAC. Given the highest $\eta_{ext,max}$ and smallest roll-off, as far as we know, the nondoped device of TCP-BP-SFAC is the best nondoped sky-blue OLED ever reported (table S5) (*31*, *32*, *48*, *49*).

To further examine their EL performances, doped OLEDs with a configuration of ITO/HATCN (5 nm)/TAPC (50 nm)/TCTA (5 nm)/*m*CP (5 nm)/*x* wt % emitter:DPEPO (20 nm)/DPEPO (5 nm)/TmPyPB (30 nm)/LiF (1 nm)/Al are fabricated (Fig. 8A), where DPEPO functions not only as an exciton blocking layer but also as a host material. A series of doped devices with different doping concentrations are fabricated to screen the optimal concentrations, which are set to 20 wt % for P-BP-SFAC and *m*CP-BP-SFAC and 25 wt % for CP-BP-SFAC and TCP-BP-SFAC finally (table S6). The doped devices of CP-BP-SFAC, *m*CP-BP-SFAC, and TCP-BP-SFAC exhibit sky-blue EL emissions with peaks in the range of 478 to 484 nm ($CIE_{x,y}$ = 0.16, 0.28) and remarkable EL efficiencies (Fig. 8, D and E, and fig. S15B). Because of the outstanding Φ_{PL} values and large $\Theta_{//}$ values, remarkable EL performance is achieved, with $\eta_{ext,max}$, $\eta_{C,max}$, and $\eta_{P,max}$ of 36.6%, 73.8 cd A^{-1}, and 72.4 lm W^{-1} for CP-BP-SFAC; 38.0%, 73.1 cd A^{-1}, and 67.5 lm W^{-1} for *m*CP-BP-SFAC; and 38.6%, 74.3 cd A^{-1}, and 68.6 lm W^{-1} for TCP-BP-SFAC (Table 2). Impressively, to the best of our knowledge, the eximious $\eta_{ext,max}$ of 38.6% is the highest value for sky-blue OLEDs reported so far (table S7) (*2*, *18*, *27*, *31*–*33*), demonstrating the great success of our molecular design.

Encouraged by the excellent EL performance of TCP-BP-SFAC, its potential application in the fabrication of white OLEDs is further explored (Fig. 9). First, the feasibility of TCP-BP-SFAC on the fully nondoped hybrid two-color white OLED is studied, which is rarely reported to date. The nondoped white OLED W1 with a configuration of ITO/HATCN (5 nm)/TAPC (50 nm)/TCTA (5 nm)/*m*CP (5 nm)/$Ir(tptpy)_2acac$ (0.05 nm)/TCP-BP-SFAC (5 nm)/$Ir(tptpy)_2acac$ (0.05 nm)/TCP-BP-SFAC (5 nm)/DPEPO (5 nm)/TmPyPB (30 nm)/LiF (1 nm)/Al is fabricated, in which iridium(III)bis(4-(4-t-butylphenyl)thieno[3,2-c]pyridinato-N,C_2)acetylacetonate ($Ir(tptpy)_2acac$) is used as the orange emitting layer and TCP-BP-SFAC functions as

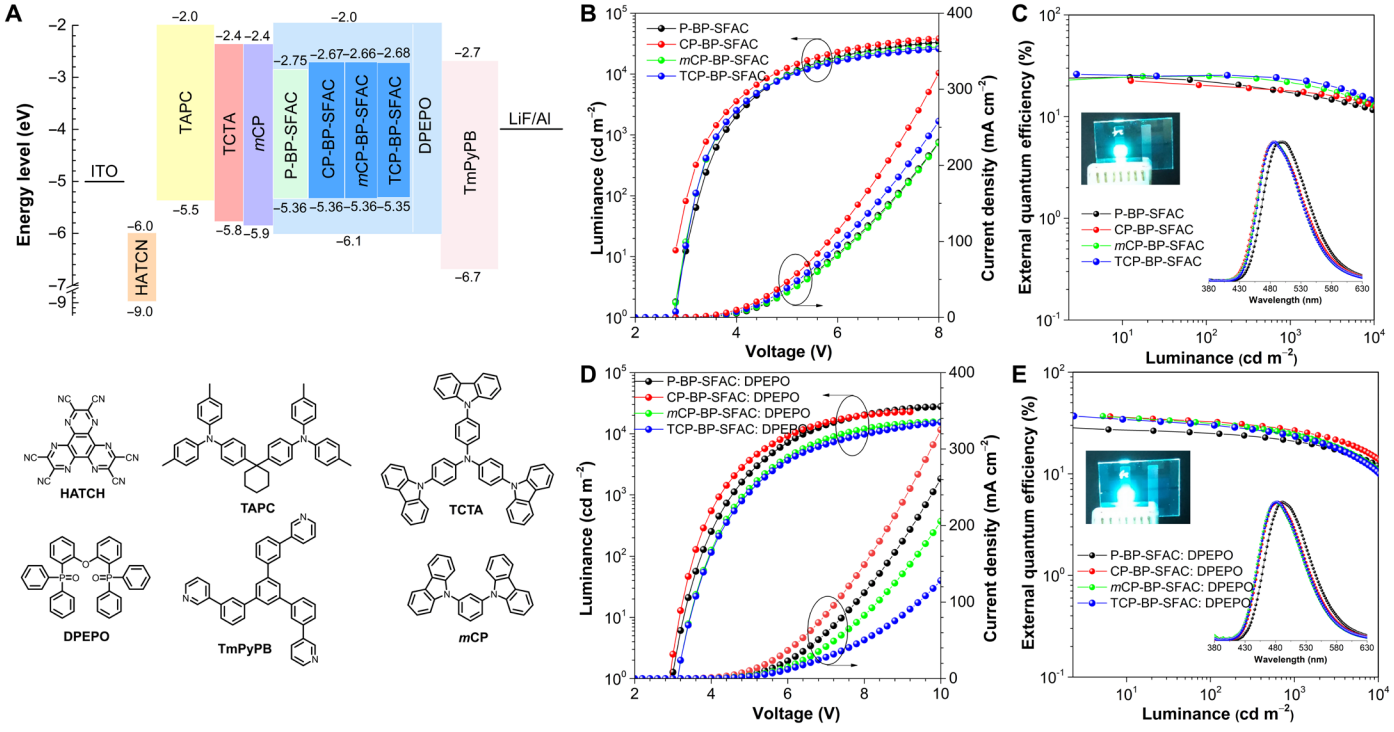

Fig. 8. Device performance of sky-blue OLEDs. (**A**) Device architecture, energy diagram, and functional layers for the vacuum-deposited OLEDs. Plots of (**B** and **D**) luminance–voltage–current density and (**C** and **E**) external quantum efficiency–luminance of nondoped and doped OLEDs. Inset in (C) and (E): EL spectra and photos (TCP-BP-SFAC) of the nondoped and doped devices at 5 V.

Table 2. EL performances for nondoped and doped OLEDs based on the new molecules. Emitting layers of doped OLEDs: 20 wt % P-BP-SFAC:DPEPO, 25 wt % CP-BP-SFAC:DPEPO, 20 wt % *m*CP-BP-SFAC:DPEPO, and 25 wt % TCP-BP-SFAC:DPEPO; V_{on}, turn-on voltage at 1 cd m^{-2}; $\eta_{C,max}$, maximum current efficiency; $\eta_{P,max}$, maximum power efficiency; $\eta_{ext,max}$, maximum external quantum efficiency; L_{max}, maximum luminance; λ_{EL}, EL peak; CIE, Commission Internationale de l'Eclairage coordinates.

Emitter	V_{on} (V)	$\eta_{C,max}$ (cd A^{-1})	$\eta_{P,max}$ (lm W^{-1})	$\eta_{ext,max}$ (%)	L_{max} (cd m^{-2})	λ_{EL} (nm)	CIE (*x*, *y*)
Nondoped OLEDs							
P-BP-SFAC	2.8	60.8	66.7	24.4	37880	500	(0.19, 0.42)
CP-BP-SFAC	2.7	51.2	57.4	22.5	39460	490	(0.19, 0.36)
*m*CP-BP-SFAC	2.8	53.8	56.0	25.0	28590	488	(0.17, 0.34)
TCP-BP-SFAC	2.7	56.4	63.3	26.1	33030	488	(0.17, 0.34)
Doped OLEDs							
P-BP-SFAC	3.0	66.6	69.7	28.9	27650	492	(0.18, 0.38)
CP-BP-SFAC	3.1	73.8	72.4	36.6	21900	484	(0.17, 0.30)
*m*CP-BP-SFAC	3.3	73.1	67.5	38.0	15880	478	(0.16, 0.28)
TCP-BP-SFAC	3.3	74.3	68.6	38.6	17130	480	(0.16, 0.28)

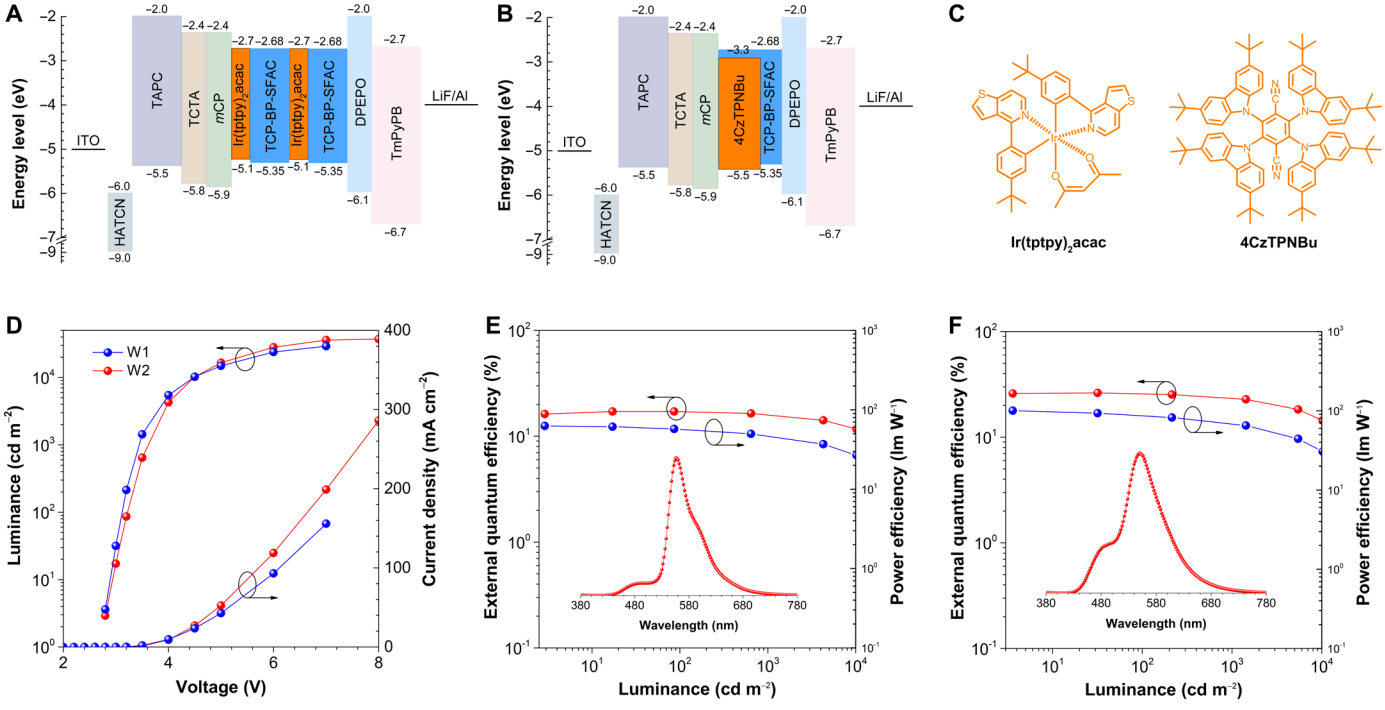

Fig. 9. Device performance of warm-white OLEDs. Device architectures and energy diagrams of (**A**) the nondoped white device and (**B**) the doped white device. (**C**) Molecular structures of Ir(tptpy)$_2$acac and 4CzTPNBu. (**D**) Luminance–voltage–current density curves of devices W1 and W2. External quantum efficiency–luminance–power efficiency curves of devices (**E**) W1 and (**F**) W2. Inset in (E) and (F): EL spectra of devices W1 and W2 at 1000 cd m^{-2}.

the blue emitting layer. Device W1 has a low turn-on voltage of 2.8 V and displays warm-white light (CIE$_{x,y}$ = 0.44, 0.52), with an L_{max} of 37310 cd A^{-2}. High $\eta_{ext,max}$, $\eta_{C,max}$, and $\eta_{P,max}$ values of 17.1%, 58.6 cd A^{-1}, and 62.6 lm W^{-1}, respectively, with a small efficiency roll of 4.1% at 1000 cd A^{-2} are obtained, which are comparable to those efficient nondoped white OLEDs in the literature. In addition, all-fluorescence two-color white OLED W2 with a single-emitting layer is further fabricated with a configuration of ITO/HATCN (5 nm)/TAPC (50 nm)/TCTA (5 nm)/*m*CP (5 nm)/0.5 wt % 2,3,5,6-tetrakis(3,6-di-(*tert*-butyl)carbazol-9-yl)-1,4-dicyanobenzene (4CzTPNBu):TCP-BP-SFAC (20 nm)/DPEPO (5 nm)/TmPyPB (30 nm)/LiF (1 nm)/Al, in which TCP-BP-SFAC serves as both blue emitter and host, and a reported TADF molecule, 4CzTPNBu, works as an orange emitter. Device W2 also shows a low turn-on voltage of 2.8 V and radiates intense warm-white light (CIE$_{x,y}$ = 0.37, 0.51) with an L_{max} of 29,190 cd m^{-2}. Notably, device W2

achieves outstanding EL efficiencies of $\eta_{ext,max}$, $\eta_{C,max}$, and $\eta_{P,max}$ values of 26.2%, 89.6 cd A^{-1}, and 100.5 lm W^{-1}, respectively, with a small efficiency roll-off of 12.9% at 1000 cd m^{-2}. To the best of our knowledge, device W2 is the most efficient all-fluorescence single-emitting layer white OLEDs reported so far (table S8) (*6*, *50*–*55*). These results further validate the success of our molecular design of robust and efficient luminescent materials for high-performance OLEDs.

DISCUSSION

In this work, an effective molecular design strategy for highly efficient luminescent molecules is proposed and a series of robust carbonyl-cored molecules with strong sky-blue delayed fluorescence are developed. In these molecules, carbonyl and SFAC form a twisted D-A framework via a phenyl bridge, which is responsible for the generation of sky-blue delayed fluorescence. The presence of carbonyl core is favored for enhancing SOC and promoting RISC because of n-π* transition, which facilitates the occurrence of delayed fluorescence. Moreover, the n orbital on carbonyl core makes the T_1 states of these molecules that are governed by n-π* transition more sensitive to the changes in matrix polarity than the S_1 states dominated with π-π* transition. In comparison with neat films, the doped films of these molecules in a DPEPO host have larger increments of T_1 energy levels than S_1 ones, leading to reduced ΔE_{ST} values. Such kind of host tuning effect associated with the different polarities and transition types of S_1 and T_1 states can be used to effectively modulate ΔE_{ST} values and regulate delayed fluorescence property.

The introduction of carbazole units on the other side of carbonyl core barely interferes the electronic structures of HOMOs and LUMOs and thus shows no destructive effect on delayed fluorescence nature, but weakens the ICT effect to some degree, rendering blue-shifted emissions of the molecules. The presence of the carbazole units not only exerts apparent positive impacts on enhancing thermal stability and preventing emission quenching and exciton annihilation but also affects the carrier mobility by regulating the distribution of HOMO-1 orbitals and the stacking of the molecules. As the increase of carbazole units, the electron mobility of the molecules changes slightly, but hole mobility shows relatively larger variations. In TCP-BP-SFAC, the hole mobility and electron mobility achieve a best balance. In addition to the incorporation of SFAC, the expansion of molecular plane containing transition dipole moment by introduction of carbazole units can further promote horizontal dipole orientation of these molecules in film sates.

The synergistic effect of the above factors endows TCP-BP-SFAC with an excellent Φ_{PL} value of 99%, a large $\Theta_{//}$ value of 88.0%, and highly balanced hole and electron mobilities. Because of these distinguished merits, outstanding $\eta_{ext,max}$ values of up to 26.1 and 38.6% are attained in the state-of-the-art sky-blue nondoped ($CIE_{x,y}$ = 0.17, 0.34) and doped ($CIE_{x,y}$ = 0.16, 0.28) OLEDs of TCP-BP-SFAC, respectively. In addition, high-performance nondoped hybrid white OLED with a $\eta_{ext,max}$ of 17.1% and a $\eta_{P,max}$ of 62.6 lm W^{-1}, and all-fluorescence single-emitting layer white OLEDs with a $\eta_{ext,max}$ of 26.2% and a $\eta_{P,max}$ of 100.5 lm W^{-1} are realized using TCP-BP-SFAC as blue emitter. These results not only eloquently demonstrate the superb competence of these luminescent molecules in OLED industry but also unveil that horizontal dipole orientation engineering of the molecules may bring about further breakthroughs in OLED researches.

MATERIALS AND METHODS

General information

All the chemicals and reagents were purchased from commercial sources and used as received without further purification. The final products were subjected to vacuum sublimation to further improve purity before PL and EL property investigations. ^1H and ^{13}C nuclear magnetic resonance (NMR) spectra were measured on a Bruker AV 500 spectrometer or a Bruker AV 400 spectrometer in $CDCl_3$, CD_2Cl_2, or C_2D_6SO at room temperature. High-resolution mass spectra were recorded on a GCT premier CAB048 mass spectrometer operating in the matrix-assisted laser desorption/ionization–time-of-flight (MALDI-TOF) mode. Ultraviolet (UV)–visible absorption spectra were measured on a Shimadzu UV-2600 spectrophotometer. PL spectra were recorded on a Horiba Fluoromax-4 spectrofluorometer. PL quantum yields were measured using a Hamamatsu absolute PL quantum yield spectrometer C11347 Quantaurus_QY. Transient PL decay spectra were measured using Quantaurus-Tau fluorescence lifetime measurement system (C11367-03, Hamamatsu Photonics Co., Japan). Cyclic voltammograms were measured in a solution of tetra-*n*-butylammonium hexafluorophosphate (nBu_4NPF_6, 0.1 M) in dichloromethane (anodic) and dimethylformamide (cathodic) at a scan rate of 50 mV s^{-1}, using a platinum wire as the auxiliary electrode, a glass carbon disk as the working electrode, and Ag/Ag^+ as the reference electrode, standardized for the redox couple ferricenium/ferrocene (Fc/Fc^+) (HOMO = −[Eonsetox +4.8] eV, and LUMO = −[Eonsetox +4.8] eV) (*56*). Eonsetox and Eonsetox represent the onset oxidation and reduction potentials relative to Fc/Fc^+, respectively. Thermogravimetric analysis (TGA) was carried out on TA TGA Q5000 under dry nitrogen at a heating rate of 20°C min^{-1}. Thermal transition was investigated by TA DSC Q1000 under dry nitrogen at a heating rate of 10°C min^{-1}. The ground-state geometries were optimized using the density functional theory (DFT) method with PBE0-D3 functional at the basis set level of 6-31G (d, p), and the excited-state geometries were optimized using the time-dependent DFT method with PBE0-D3 functional at the basis set level of 6-31G (d, p). The ΔE_{ST} values were calculated by the vertical excitation based on S_0 geometry. The above calculations were performed using Gaussian16 package. The spin-density distributions of T_1 states, the length, width, and height of P-BP-SFAC, CP-BP-SFAC, *m*CP-BP-SFAC, and TCP-BP-SFAC, the MPI values, and natural transition orbital analysis were analyzed with Multiwfn (*57*).

Synthesis and characterization

P-BP-SFAC, CP-BP-SFAC, *m*CP-BP-SFAC, and TCP-BP-SFAC were synthesized and characterized according to the methods described in fig. S1. The detailed procedures and characterization data are given in the Supplementary Materials.

Horizontal dipole ratio measurement

For the measurement of orientation of emitting dipoles in molecules, a setup RSQX-01 made by Changchun Ruoshui Technology Development Co. Ltd. was used. The dipole orientation of doped and nondoped films was determined by angle-resolved and polarization-resolved PL on a half quartz cylinder prism. A continuous-wave He:Cd laser (325 nm) with a fixed angle of 45° to the substrate was used as excitation source. *p*-Polarized emitted light was detected at the respective peak wavelength of the PL spectrum of each film.

Carrier mobility measurement

The SCLC property can be described via the Mott-Gurney equation (Eq. 1), and the carrier mobility (μ) of organic semiconductors can be calculated according to the Poole-Frenkel formula (Eq. 2), where ε_0 is the free-space permittivity (8.85×10^{-14} C V^{-1} cm^{-1}), ε_r is the relative dielectric constant (assumed to be 3.0 for organic semiconductors), E is the electric field, μ_0 is the zero-field mobility, γ is the Poole-Frenkel factor, and L is the thickness of the neat film of each molecule

$$J = \frac{9}{8}\varepsilon_0\varepsilon_r\mu\frac{E^2}{L} = \frac{9}{8}\varepsilon_0\varepsilon_r\frac{V^2}{L^3}\mu_0\exp\left(0.891\gamma\sqrt{\frac{V}{L}}\right) \quad (1)$$

$$\mu = \mu_0\exp(\gamma\sqrt{E}) \quad (2)$$

By fitting the current density–voltage curves in the SCLC region according to Eq. 1 (*58*), the μ_0 and γ values are obtained, thus generating the field-dependent carrier mobility by Eq. 2.

OLED fabrication and measurement

The glass substrates precoated with a 90-nm layer of ITO with a sheet resistance of 15 to 20 ohms per square were successively cleaned in ultrasonic bath of acetone, isopropanol, detergent, and deionized water, respectively, taking 10 min for each step. Then, the substrates were completely dried in a 70°C oven. Before the fabrication processes, to improve the hole injection ability of ITO, the substrates were treated by O_2 plasma for 10 min. The vacuum-deposited OLEDs were fabricated under a pressure of $<5 \times 10^{-4}$ Pa in a Fangsheng OMV-FS450 vacuum deposition system. Organic materials, LiF, and Al were deposited at rates of 1 to 2 A s^{-1}, 0.1 A s^{-1}, and 5 A s^{-1}, respectively. The effective emitting area of the device was 9 mm^2, determined by the overlap between anode and cathode. The luminance–voltage–current density and external quantum efficiency were characterized with a dual-channel Keithley 2614B source meter and a PIN-25D silicon photodiode. The EL spectra were obtained via an Ocean Optics USB 2000+ spectrometer, along with a Keithley 2614B source meter. For white OLEDs, the luminance–voltage–current density characteristics and electroluminescent spectra were obtained using a PhotoResearch PR670 spectroradiometer, with a Keithley 2400 source meter. All the characterizations were conducted at room temperature in ambient conditions without any encapsulation, as soon as the devices were fabricated.

SUPPLEMENTARY MATERIALS

Supplementary material for this article is available at https://science.org/doi/10.1126/sciadv.abj2504

REFERENCES AND NOTES

1. C. W. Tang, S. A. VanSlyke, Organic electroluminescent diodes. *Appl. Phys. Lett.* **51**, 913–915 (1987).
2. D. H. Ahn, S. W. Kim, H. Lee, I. J. Ko, D. Karthik, J. Y. Lee, J. H. Kwon, Highly efficient blue thermally activated delayed fluorescence emitters based on symmetrical and rigid oxygen-bridged boron acceptors. *Nat. Photonics* **13**, 540–546 (2019).
3. S. Hirata, Y. Sakai, K. Masui, H. Tanaka, S. Y. Lee, H. Nomura, N. Nakamura, M. Yasumatsu, H. Nakanotani, Q. Zhang, K. Shizu, H. Miyazaki, C. Adachi, Highly efficient blue electroluminescence based on thermally activated delayed fluorescence. *Nat. Mater.* **14**, 330–336 (2015).
4. X. Tang, L. S. Cui, H. C. Li, A. J. Gillett, F. Auras, Y. K. Qu, C. Zhong, S. T. E. Jones, Z. Q. Jiang, R. H. Friend, L. S. Liao, Highly efficient luminescence from space-confined charge-transfer emitters. *Nat. Mater.* **19**, 1332–1338 (2020).
5. T.-L. Wu, M.-J. Huang, C.-C. Lin, P.-Y. Huang, T.-Y. Chou, R.-W. Chen-Cheng, H.-W. Lin, R.-S. Liu, C.-H. Cheng, Diboron compound-based organic light-emitting diodes with high efficiency and reduced efficiency roll-off. *Nat. Photonics* **12**, 235–240 (2018).
6. C. Zhang, Y. Lu, Z. Liu, Y. Zhang, X. Wang, D. Zhang, L. Duan, A π-D and π-A exciplex-forming host for high-efficiency and long-lifetime single-emissive-layer fluorescent white organic light-emitting diodes. *Adv. Mater.* **32**, 2004040 (2020).
7. M. Y. Wong, E. Zysman-Colman, Purely organic thermally activated delayed fluorescence materials for organic light-emitting diodes. *Adv. Mater.* **29**, 1605444 (2017).
8. J. Rao, L. Yang, X. Li, L. Zhao, S. Wang, J. Ding, L. Wang, Meta junction promoting efficient thermally activated delayed fluorescence in donor-acceptor conjugated polymers. *Angew. Chem. Int. Ed.* **59**, 17903–17909 (2020).
9. F. B. Dias, J. Santos, D. R. Graves, P. Data, R. S. Nobuyasu, M. A. Fox, A. S. Batsanov, T. Palmeira, M. N. Berberan-Santos, M. R. Bryce, A. P. Monkman, The role of local triplet excited states and D-A relative orientation in thermally activated delayed fluorescence: Photophysics and devices. *Adv. Sci.* **3**, 1600080 (2016).
10. S. Shao, L. Wang, Through-space charge transfer polymers for solution-processed organic light-emitting diodes. *Aggregate* **1**, 45–56 (2020).
11. J.-M. Teng, Y.-F. Wang, C.-F. Chen, Recent progress of narrowband TADF emitters and their applications in OLEDs. *J. Mater. Chem. C* **8**, 11340–11353 (2020).
12. M. Godumala, J. Hwang, H. Kang, J.-E. Jeong, A. K. Harit, M. J. Cho, H. Y. Woo, S. Park, D. H. Choi, High-performance, solution-processable thermally activated delayed fluorescent organic light-emitting diodes realized via the adjustment of the composition of the organoboron acceptor monomer in copolymer host materials. *ACS Appl. Mater. Interfaces* **12**, 35300–35310 (2020).
13. H. Uoyama, K. Goushi, K. Shizu, H. Nomura, C. Adachi, Highly efficient organic light-emitting diodes from delayed fluorescence. *Nature* **492**, 234–238 (2012).
14. C. Y. Kim, C. Lee, H. J. Kim, J. Hwang, M. Godumala, J.-E. Jeong, H. Y. Woo, M. J. Cho, S. Park, D. H. Choi, Achievement of high efficiency with extremely low efficiency roll-off in solution-processed thermally activated delayed fluorescence OLEDs manufactured using xanthone-based bipolar host materials. *J. Mater. Chem. C* **8**, 6780–6787 (2020).
15. P. Rajamalli, N. Senthilkumar, P.-Y. Huang, C.-C. Ren-Wu, H.-W. Lin, C.-H. Cheng, New molecular design concurrently providing superior pure blue, thermally activated delayed fluorescence and optical out-coupling efficiencies. *J. Am. Chem. Soc.* **139**, 10948–10951 (2017).
16. J. W. Sun, J.-H. Lee, C.-K. Moon, K.-H. Kim, H. Shin, J.-J. Kim, A fluorescent organic light-emitting diode with 30% external quantum efficiency. *Adv. Mater.* **26**, 5684–5688 (2014).
17. H. Kaji, H. Suzuki, T. Fukushima, K. Shizu, K. Suzuki, S. Kubo, T. Komino, H. Oiwa, F. Suzuki, A. Wakamiya, Y. Murata, C. Adachi, Purely organic electroluminescent material realizing 100% conversion from electricity to light. *Nat. Commun.* **6**, 8476 (2015).
18. Y. Qu, J. Kim, C. Coburn, S. R. Forrest, Efficient, nonintrusive outcoupling in organic light emitting devices using embedded microlens arrays. *ACS Photonics* **5**, 2453–2458 (2018).
19. D. Yuan, B. Liu, Z. Zhu, Y. Guo, C. Cheng, H. Chen, M. Gu, M. Xu, L. Chen, J. Liu, X. Ouyang, Directional control and enhancement of light output of scintillators by using microlens arrays. *ACS Appl. Mater. Interfaces* **12**, 29473–29480 (2020).
20. S. Chen, Z. Zhao, B. Z. Tang, H.-S. Kwok, Growth methods, enhanced photoluminescence, high hydrophobicity and light scattering of 4,4′-bis(1,2,2-triphenylvinyl)biphenyl nanowires. *Org. Electron.* **13**, 1996–2002 (2012).
21. T. E. Umbach, S. Röllgen, S. Schneider, H. Klesper, A. M. Umbach, K. Meerholz, Low-refractive index layers in organic light-emitting diodes via electrospray deposition for enhanced outcoupling efficiencies. *Adv. Eng. Mater.* **22**, 1900897 (2020).
22. W. Youn, J. W. Lee, H. Yu, D. Y. Kim, Effect of refractive index contrast on out-coupling efficiency of corrugated OLEDs using low-refractive-index LiF interlayer. *ACS Appl. Electron. Mater.* **2**, 2218–2223 (2020).
23. C.-Y. Chen, W.-K. Lee, Y.-J. Chen, C.-Y. Lu, H. Y. Lin, C.-C. Wu, Enhancing optical out-coupling of organic light-emitting devices with nanostructured composite electrodes consisting of indium tin oxide nanomesh and conducting polymer. *Adv. Mater.* **27**, 4883–4888 (2015).
24. T.-A. Lin, T. Chatterjee, W.-L. Tsai, W.-K. Lee, M.-J. Wu, M. Jiao, K.-C. Pan, C.-L. Yi, C.-L. Chung, K.-T. Wong, C.-C. Wu, Sky-blue organic light emitting diode with 37% external quantum efficiency using thermally activated delayed fluorescence from spiroacridine-triazine hybrid. *Adv. Mater.* **28**, 6976–6983 (2016).
25. M. Liu, R. Komatsu, X. Cai, K. Hotta, S. Sato, K. Liu, D. Chen, Y. Kato, H. Sasabe, S. Ohisa, Y. Suzuri, D. Yokoyama, S.-J. Su, J. Kido, Horizontally orientated sticklike emitters: Enhancement of intrinsic out-coupling factor and electroluminescence performance. *Chem. Mater.* **29**, 8630–8636 (2017).
26. X. Gong, P. Li, Y.-H. Huang, C.-Y. Wang, C.-H. Lu, W.-K. Lee, C. Zhong, Z. Chen, W. Ning, C.-C. Wu, S. Gong, C. Yang, A red thermally activated delayed fluorescence emitter simultaneously having high photoluminescence quantum efficiency and preferentially horizontal emitting dipole orientation. *Adv. Funct. Mater.* **30**, 1908839 (2020).
27. H. Lim, H. J. Cheon, S.-J. Woo, S.-K. Kwon, Y.-H. Kim, J.-J. Kim, Highly efficient deep-blue OLEDs using a TADF emitter with a narrow emission spectrum and high horizontal emitting dipole ratio. *Adv. Mater.* **32**, 2004083 (2020).

28. C. Mayr, S. Y. Lee, T. D. Schmidt, T. Yasuda, C. Adachi, W. Brütting, Efficiency enhancement of organic light-emitting diodes incorporating a highly oriented thermally activated delayed fluorescence emitter. *Adv. Funct. Mater.* **24**, 5232–5239 (2014).
29. Y. Xiang, P. Li, S. Gong, Y.-H. Huang, C.-Y. Wang, C. Zhong, W. Zeng, Z. Chen, W.-K. Lee, X. Yin, C.-C. Wu, C. Yang, Acceptor plane expansion enhances horizontal orientation of thermally activated delayed fluorescence emitters. *Sci. Adv.* **6**, eaba7855 (2020).
30. S. Y. Byeon, J. Kim, D. R. Lee, S. H. Han, S. R. Forrest, J. Y. Lee, Nearly 100% horizontal dipole orientation and upconversion efficiency in blue thermally activated delayed fluorescent emitters. *Adv. Opt. Mater.* **6**, 1701340 (2018).
31. W. Li, B. Li, X. Cai, L. Gan, Z. Xu, W. Li, K. Liu, D. Chen, S.-J. Su, Tri-spiral donor for high efficiency and versatile blue thermally activated delayed fluorescence materials. *Angew. Chem. Int. Ed.* **58**, 11301–11305 (2019).
32. W. Li, W. Li, L. Gan, M. Li, N. Zheng, C. Ning, D. Chen, Y.-C. Wu, S.-J. Su, J-aggregation enhances the electroluminescence performance of a sky-blue thermally activated delayed-fluorescence emitter in nondoped organic light-emitting diodes. *ACS Appl. Mater. Interfaces* **12**, 2717–2723 (2020).
33. W. Li, M. Li, W. Li, Z. Xu, L. Gan, K. Liu, N. Zheng, C. Ning, D. Chen, Y.-C. Wu, S.-J. Su, Spiral donor design strategy for blue thermally activated delayed fluorescence emitters. *ACS Appl. Mater. Interfaces* **13**, 5302–5311 (2021).
34. H. Ma, Q. Peng, Z. An, W. Huang, Z. Shuai, Efficient and long-lived room-temperature organic phosphorescence: Theoretical descriptors for molecular designs. *J. Am. Chem. Soc.* **141**, 1010–1015 (2019).
35. J. Guo, J. Fan, L. Lin, J. Zeng, H. Liu, C.-K. Wang, Z. Zhao, B. Z. Tang, Mechanical insights into aggregation-induced delayed fluorescence materials with anti-kasha behavior. *Adv. Sci.* **6**, 1801629 (2018).
36. Q. Zhang, B. Li, S. Huang, H. Nomura, H. Tanaka, C. Adachi, Efficient blue organic light-emitting diodes employing thermally activated delayed fluorescence. *Nat. Photonics* **8**, 326–332 (2014).
37. H. Liu, J. Zeng, J. Guo, H. Nie, Z. Zhao, B. Z. Tang, High-performance non-doped OLEDs with nearly 100% exciton use and negligible efficiency roll-off. *Angew. Chem. Int. Ed.* **57**, 9290–9294 (2018).
38. J. Huang, H. Nie, J. Zeng, Z. Zhuang, S. Gan, Y. Cai, J. Guo, S.-J. Su, Z. Zhao, B. Z. Tang, Highly efficient nondoped OLEDs with negligible efficiency roll-off fabricated from aggregation-induced delayed fluorescence luminogens. *Angew. Chem. Int. Ed.* **56**, 12971–12976 (2017).
39. J. Chen, J. Zeng, X. Zhu, J. Guo, Z. Zhao, B. Z. Tang, Versatile aggregation-enhanced delayed fluorescence luminogens functioning as emitters and hosts for high-performance organic light-emitting diodes. *CCS Chem.* **3**, 230–240 (2021).
40. L.-S. Cui, A. J. Gillett, S.-F. Zhang, H. Ye, Y. Liu, X.-K. Chen, Z.-S. Lin, E. W. Evans, W. K. Myers, T. K. Ronson, H. Nakanotani, S. Reineke, J.-L. Bredas, C. Adachi, R. H. Friend, Fast spin-flip enables efficient and stable organic electroluminescence from charge-transfer states. *Nat. Photonics* **14**, 636–642 (2020).
41. X. Cai, B. Gao, X.-L. Li, Y. Cao, S.-J. Su, Singlet-triplet splitting energy management via acceptor substitution: Complanation molecular design for deep-blue thermally activated delayed fluorescence emitters and organic light-emitting diodes application. *Adv. Funct. Mater.* **26**, 8042–8052 (2016).
42. Q. Peng, Z. Shuai, Molecular mechanism of aggregation-induced emission. *Aggregate* , (2021).
43. H. Geng, X. Zheng, Z. Shuai, L. Zhu, Y. Yi, Understanding the charge transport and polarities in organic donor-acceptor mixed-stack crystals: Molecular insights from the super-exchange couplings. *Adv. Mater.* **27**, 1443–1449 (2015).
44. R. Sato, T. Kawamoto, T. Mori, Asymmetrical hole/electron transport in donor–acceptor mixed-stack cocrystals. *J. Mater. Chem. C* **7**, 567–577 (2019).
45. W. Kohn, A. D. Becke, R. G. Parr, Density functional theory of electronic structure. *J. Phys. Chem.* **100**, 12974–12980 (1996).
46. C. Han, Y. Zhao, H. Xu, J. Chen, Z. Deng, D. Ma, Q. Li, P. Yan, A simple phosphine–oxide host with a multi-insulating structure: High triplet energy level for efficient blue electrophosphorescence. *Chem. Eur. J.* **17**, 5800–5803 (2011).
47. R. J. Holmes, S. R. Forrest, Y. J. Tung, R. C. Kwong, J. J. Brown, S. Garon, M. E. Thompson, Blue organic electrophosphorescence using exothermic host–guest energy transfer. *Appl. Phys. Lett.* **82**, 2422–2424 (2003).
48. I. S. Park, K. Matsuo, N. Aizawa, T. Yasuda, High-performance dibenzoheteraborin-based thermally activated delayed fluorescence emitters: Molecular architectonics for concurrently achieving narrowband emission and efficient triplet-singlet spin conversion. *Adv. Funct. Mater.* **28**, 1802031 (2018).
49. Y.-Z. Shi, K. Wang, X. Li, G.-L. Dai, W. Liu, K. Ke, M. Zhang, S.-L. Tao, C.-J. Zheng, X.-M. Ou, X.-H. Zhang, Intermolecular charge-transfer transition emitter showing thermally activated delayed fluorescence for efficient non-doped OLEDs. *Angew. Chem. Int. Ed.* **57**, 9480–9484 (2018).
50. X. Tang, Y. Li, Y. K. Qu, C. C. Peng, A. Khan, Z.-Q. Jiang, L.-S. Liao, All-fluorescence white organic light-emitting diodes exceeding 20% EQEs by rational manipulation of singlet and triplet excitons. *Adv. Funct. Mater.* **30**, 1910633 (2020).
51. W. Liu, C.-J. Zheng, K. Wang, M. Zhang, D.-Y. Chen, S.-L. Tao, F. Li, Y.-P. Dong, C.-S. Lee, X.-M. Ou, X.-H. Zhang, High performance all fluorescence white organic light emitting devices with a highly simplified structure based on thermally activated delayed fluorescence dopants and host. *ACS Appl. Mater. Interfaces* **8**, 32984–32991 (2016).
52. J. Sun, J. Zhang, Q. Liang, Y. Wei, C. Duan, C. Han, H. Xu, Charge-transfer exciton manipulation based on hydrogen bond for efficient white thermally activated delayed fluorescence. *Adv. Funct. Mater.* **30**, 1908568 (2020).
53. Z. Wu, Y. Liu, C. Zhao, D. Yang, X. Qiao, J. Chen, C. Yang, H. Kleemann, K. Leo, D. Ma, Strategic-tuning of radiative excitons for efficient and stable fluorescent white organic light-emitting diodes. *Nat. Commun.* **10**, 2380 (2019).
54. D. Ding, Z. Wang, C. Li, J. Zhang, C. Duan, Y. Wei, H. Xu, Highly efficient and color-stable thermally activated delayed fluorescence white light-emitting diodes featured with single-doped single emissive layers. *Adv. Mater.* **32**, 1906950 (2020).
55. H. Liu, J. Chen, Y. Fu, Z. Zhao, B. Z. Tang, Achieving high electroluminescence efficiency and high color rendering index for all-fluorescent white OLEDs based on an out-of-phase sensitizing system. *Adv. Funct. Mater.* **31**, 2103273 (2021).
56. L. Leonat, G. Sbarcea, I. V. Branzoi, Cyclic voltammetry for energy levels estimation of organic materials. *U.P.B. Sci. Bull. Ser. B* **75**, 111–118 (2013).
57. T. Lu, F. Chen, Multiwfn: A multifunctional wavefunction analyzer. *J. Comput. Chem.* **33**, 580–592 (2012).
58. Z. S. An, J. S. Yu, S. C. Jones, S. Barlow, S. Yoo, B. Domercq, P. Prins, L. D. A. Siebbeles, B. Kippelen, S. R. Marder, High electron mobility in room-temperature discotic liquid-crystalline perylene diimides. *Adv. Mater.* **17**, 2580–2583 (2015).
59. X. Zheng, R. Huang, C. Zhong, G. Xie, W. Ning, M. Huang, F. Ni, F. B. Dias, C. Yang, Achieving 21% external quantum efficiency for nondoped solution-processed sky-blue thermally activated delayed fluorescence OLEDs by means of multi-(donor/acceptor) emitter with through-space/-bond charge transfer. *Adv. Sci.* **7**, 1902087 (2020).
60. Q. Zhang, D. Tsang, H. Kuwabara, Y. Hatae, B. Li, T. Takahashi, S. Y. Lee, T. Yasuda, C. Adachi, Nearly 100% internal quantum efficiency in undoped electroluminescent devices employing pure organic emitters. *Adv. Mater.* **27**, 2096–2100 (2015).
61. X. L. Chen, J. H. Jia, R. Yu, J. Z. Liao, M. X. Yang, C. Z. Lu, Combining charge-transfer pathways to achieve unique thermally activated delayed fluorescence emitters for high-performance solution-processed, non-doped blue OLEDs. *Angew. Chem. Int. Ed.* **56**, 15006–15009 (2017).
62. D. Chen, K. Liu, X. Li, B. Li, M. Liu, X. Cai, Y. Ma, Y. Cao, S.-J. Su, Engineering the excited-state properties of purely organic intramolecular and intermolecular charge transfer emitters towards high-performance fluorescent OLEDs. *J. Mater. Chem. C* **5**, 10991–11000 (2017).
63. K. Wu, Z. Wang, L. Zhan, C. Zhong, S. Gong, G. Xie, C. Yang, Realizing highly efficient solution-processed homojunction-like sky-blue OLEDs by using thermally activated delayed fluorescent emitters featuring an aggregation-induced emission property. *J. Phys. Chem. Lett.* **9**, 1547–1553 (2018).
64. J. Huang, Z. Xu, Z. Cai, J. Guo, J. Guo, P. Shen, Z. Wang, Z. Zhao, D. Ma, B. Z. Tang, Robust luminescent small molecules with aggregation-induced delayed fluorescence for efficient solution-processed OLEDs. *J. Mater. Chem. C* **7**, 330–339 (2019).
65. P. Ganesan, D.-G. Chen, J.-L. Liao, W.-C. Li, Y.-N. Lai, D. Luo, C.-H. Chang, C.-L. Ko, W.-Y. Hung, S.-W. Liu, G.-H. Lee, P.-T. Chou, Y. Chi, Isomeric spiro-[acridine-9,9′-fluorene]-2,6-dipyridylpyrimidine based TADF emitters: Insights into photophysical behaviors and OLED performances. *J. Mater. Chem. C* **6**, 10088–10100 (2018).
66. J. Jayakumar, T. L. Wu, M. J. Huang, P. Y. Huang, T. Y. Chou, H. W. Lin, C. H. Cheng, Pyridine-carbonitrile-carbazole-based delayed fluorescence materials with highly congested structures and excellent OLED performance. *ACS Appl. Mater. Interfaces* **11**, 21042–21048 (2019).
67. C. Li, C. Duan, C. Han, H. Xu, Secondary acceptor optimization for full-exciton radiation: Toward sky-blue thermally activated delayed fluorescence diodes with external quantum efficiency of ≈30%. *Adv. Mater.* **30**, 1804228 (2018).
68. W. Huang, M. Einzinger, A. Maurano, T. Zhu, J. Tiepelt, C. Yu, H. S. Chae, T. Van Voorhis, M. A. Baldo, S. L. Buchwald, Large increase in external quantum efficiency by dihedral angle tuning in a sky-blue thermally activated delayed fluorescence emitter. *Adv. Opt. Mater.* **7**, 1900476 (2019).
69. D. R. Lee, M. Kim, S. K. Jeon, S. H. Hwang, C. W. Lee, J. Y. Lee, Design strategy for 25% external quantum efficiency in green and blue thermally activated delayed fluorescent devices. *Adv. Mater.* **27**, 5861–5867 (2015).
70. Q. Zhang, S. Sun, X. Lv, W. Liu, H. Zeng, R. Guo, S. Ye, P. Leng, S. Xiang, L. Wang, Manipulating the positions of CH···N in acceptors of pyrimidine–pyridine hybrids for highly efficient sky-blue thermally activated delayed fluorescent OLEDs. *Mater. Chem. Front.* **2**, 2054–2062 (2018).
71. J. W. Sun, K. H. Kim, C. K. Moon, J. H. Lee, J. J. Kim, Highly efficient sky-blue fluorescent organic light emitting diode based on mixed cohost system for thermally activated delayed fluorescence emitter (2CzPN). *ACS Appl. Mater. Interfaces* **8**, 9806–9810 (2016).

72. H. Sasabe, N. Onuma, Y. Nagai, T. Ito, J. Kido, High power efficiency blue-to-green organic light-emitting diodes using isonicotinonitrile-based fluorescent emitters. *Chem. Asian J.* **12**, 648–654 (2017).
73. D. Zhang, M. Cai, Y. Zhang, D. Zhang, L. Duan, Sterically shielded blue thermally activated delayed fluorescence emitters with improved efficiency and stability. *Mater. Horiz.* **3**, 145–151 (2016).
74. F. Ni, C.-W. Huang, Y. Tang, Z. Chen, Y. Wu, S. Xia, X. Cao, J.-H. Hsu, W.-K. Lee, K. Zheng, Z. Huang, C.-C. Wu, C. Yang, Integrating molecular rigidity and chirality into thermally activated delayed fluorescence emitters for highly efficient sky-blue and orange circularly polarized electroluminescence. *Mater. Horiz.* **8**, 547–555 (2021).
75. T. Ohsawa, H. Sasabe, T. Watanabe, K. Nakao, R. Komatsu, Y. Hayashi, Y. Hayasaka, J. Kido, A series of imidazo[1,2-f]phenanthridine-based sky-blue TADF emitters realizing EQE of over 20%. *Adv. Opt. Mater.* **7**, 1801282 (2019).
76. R. Yang, Q. Guan, Z. Liu, W. Song, L. Hong, T. Lei, Q. Wei, R. Peng, X. Fan, Z. Ge, A methodological study on tuning the thermally activated delayed fluorescent performance by molecular constitution in acridine-benzophenone derivatives. *Chem. Asian J.* **13**, 1187–1191 (2018).
77. X.-D. Zhu, Q.-S. Tian, Q. Zheng, X.-C. Tao, Y. Yuan, Y.-J. Yu, Y. Li, Z.-Q. Jiang, L.-S. Liao, A sky-blue thermally activated delayed fluorescence emitter based on multimodified carbazole donor for efficient organic light-emitting diodes. *Org. Electron.* **68**, 113–120 (2019).

Acknowledgments

Funding: This work was financially supported by the National Natural Science Foundation of China (21788102) and the Natural Science Foundation of Guangdong Province (2019B030301003). **Author contributions:** Z.Z. conceived of the study. Y.F. synthesized, characterized, and performed the theoretical simulation of the molecules. H.L. fabricated and characterized the devices. D.Y. and D.M. offered their helps in horizontal dipole ratio measurement. Y.F. and Z.Z. wrote and revised the manuscript. Z.Z. and B.Z.T. supervised the project and designed the experiments. All authors discussed the results and commented on the manuscript. **Competing interests:** The authors declare that they have no competing interests. **Data and materials availability:** All data needed to evaluate the conclusions in the paper are present in the paper and/or the Supplementary Materials.

Submitted 30 April 2021
Accepted 30 August 2021
Published 20 October 2021
10.1126/sciadv.abj2504

Citation: Y. Fu, H. Liu, D. Yang, D. Ma, Z. Zhao, B. Z. Tang, Boosting external quantum efficiency to 38.6% of sky-blue delayed fluorescence molecules by optimizing horizontal dipole orientation. *Sci. Adv.* **7**, eabj2504 (2021).

ScienceAdvances

Boosting external quantum efficiency to 38.6% of sky-blue delayed fluorescence molecules by optimizing horizontal dipole orientation

Yan FuHao LiuDezhi YangDongge MaZujin ZhaoBen Zhong Tang

Sci. Adv., 7 (43), eabj2504. • DOI: 10.1126/sciadv.abj2504

Science Advances (ISSN) is published by the American Association for the Advancement of Science. 1200 New York Avenue NW, Washington, DC 20005. The title *Science Advances* is a registered trademark of AAAS.